Manipulation of ionized impurity scattering for achieving high thermoelectric performance in n-type Mg_3Sb_2-based materials

Jun Mao[a,b,c,1], Jing Shuai[a,b,1], Shaowei Song[a,b,1], Yixuan Wu[d], Rebecca Dally[e,f], Jiawei Zhou[g], Zihang Liu[a,b], Jifeng Sun[h], Qinyong Zhang[i,j], Clarina dela Cruz[k], Stephen Wilson[e], Yanzhong Pei[d], David J. Singh[h], Gang Chen[g], Ching-Wu Chu[a,b,2], and Zhifeng Ren[a,b,2]

[a]Department of Physics, University of Houston, Houston, TX 77204; [b]Texas Center for Superconductivity, University of Houston, Houston, TX 77204; [c]Department of Mechanical Engineering, University of Houston, Houston, TX 77204; [d]School of Materials Science and Engineering, Tongji University, Shanghai 201804, China; [e]Materials Department, University of California, Santa Barbara, CA 93106; [f]Department of Physics, Boston College, Chestnut Hill, MA 02467; [g]Department of Mechanical Engineering, Massachusetts Institute of Technology, Cambridge, MA 02139; [h]Department of Physics and Astronomy, University of Missouri, Columbia, MO 65211; [i]Key Laboratory of Fluid and Power Machinery of Ministry of Education, Xihua University, Chengdu, Sichuan 610039, China; [j]Center for Advanced Materials and Energy, Xihua University, Chengdu, Sichuan 610039, China; and [k]Quantum Condensed Matter Division, Oak Ridge National Laboratory, Oak Ridge, TN 37831

Contributed by Ching-Wu Chu, August 24, 2017 (sent for review July 3, 2017; reviewed by Renkun Chen and Lidong Zhao)

Achieving higher carrier mobility plays a pivotal role for obtaining potentially high thermoelectric performance. In principle, the carrier mobility is governed by the band structure as well as by the carrier scattering mechanism. Here, we demonstrate that by manipulating the carrier scattering mechanism in n-type Mg_3Sb_2-based materials, a substantial improvement in carrier mobility, and hence the power factor, can be achieved. In this work, Fe, Co, Hf, and Ta are doped on the Mg site of $Mg_{3.2}Sb_{1.5}Bi_{0.49}Te_{0.01}$, where the ionized impurity scattering crosses over to mixed ionized impurity and acoustic phonon scattering. A significant improvement in Hall mobility from ∼16 to ∼81 $cm^2 \cdot V^{-1} \cdot s^{-1}$ is obtained, thus leading to a notably enhanced power factor of ∼13 $\mu W \cdot cm^{-1} \cdot K^{-2}$ from ∼5 $\mu W \cdot cm^{-1} \cdot K^{-2}$. A simultaneous reduction in thermal conductivity is also achieved. Collectively, a figure of merit (*ZT*) of ∼1.7 is obtained at 773 K in $Mg_{3.1}Co_{0.1}Sb_{1.5}Bi_{0.49}Te_{0.01}$. The concept of manipulating the carrier scattering mechanism to improve the mobility should also be applicable to other material systems.

thermoelectric | carrier scattering mechanism | ionized impurity scattering | n-type Mg_3Sb_2 | defects

Thermoelectric devices that can directly convert heat into electricity, and vice versa, can be used in waste heat recovery and cooling applications (1–3). This solid-state conversion technology has advantages in terms of its compactness for high power density, its capability to provide cleaner energy, and its long lifetime. However, the relatively low efficiency of thermoelectric modules has limited their application to niche markets. The efficiency of thermoelectric devices is determined by the Carnot efficiency and the material's figure of merit (ZT), which is defined as $ZT = (S^2\sigma/\kappa)T$, where S is the Seebeck coefficient, σ is the electrical conductivity, κ is the thermal conductivity ($\kappa = \kappa_{ele} + \kappa_{lat}$, where κ_{ele} is the electronic part and κ_{lat} is the lattice part), and T is the absolute temperature (4–6).

The challenge of improving the ZT lies in the fact that the thermoelectric parameters S, σ, and κ_{ele} are strongly interdependent (7). Therefore, two basic approaches have been used to enhance the ZT via decreasing the relatively independent lattice thermal conductivity or increasing the power factor (i.e., $S^2\sigma$). Phonon scattering via defect engineering [point defects (8–11), dislocations (12–15), and grain boundaries (16, 17)] or nanostructuring (18) has led to a significant reduction in lattice thermal conductivity. On the other hand, power factors have also been enhanced via different approaches such as band engineering (19–22), inducing resonant levels (23), the carrier filtering effect (24–27), ionized impurity scattering (28), and modulation doping (29, 30).

Generally, power factors have been optimized by tuning the carrier concentration so that a compromise between the Seebeck coefficient and the electrical conductivity is reached. Strategies for further improving power factors have mainly focused on enhancing the Seebeck coefficient (e.g., resonant levels, the carrier filtering effect, ionized impurity scattering), while a few have been aimed at boosting the mobility (e.g., modulation doping). However, Seebeck coefficient enhancement is usually accompanied by a noticeable reduction in carrier mobility (23, 28), which deteriorates the electrical conductivity, and therefore results in limited power factor improvement. In fact, the importance of increasing mobility to improve the power factor should be recognized. Its importance can be understood from the fact that since the Seebeck coefficient is strongly coupled with the electrical conductivity via carrier concentration rather than mobility, the improved mobility will monotonously increase the electrical conductivity without affecting the Seebeck coefficient, thus substantially improving the power factor.

The carrier mobility, μ, can be expressed as follows (31):

$$\mu = \frac{e\langle\tau\rangle}{m^*}, \quad [1]$$

where e is the electron charge, m^* is the effective mass, and $\langle\tau\rangle$ is the average relaxation time. In the simplest case, the relaxation

Significance

Higher carrier mobility can contribute to a larger power factor, so it is important to identify effective means for achieving higher carrier mobility. Since carrier mobility is governed by the band structure and the carrier scattering mechanism, its possible enhancement could be obtained by manipulating either or both of these. Here, we report a substantial enhancement in carrier mobility by tuning the carrier scattering mechanism in n-type Mg_3Sb_2-based materials. The ionized impurity scattering in these materials has been shifted into mixed scattering by acoustic phonons and ionized impurities. Our results clearly demonstrate that the strategy of tuning the carrier scattering mechanism is quite effective for improving the mobility and should also be applicable to other material systems.

Author contributions: J.M., C.-W.C., and Z.R. designed research; J.M., J. Shuai, and S.S. performed research; Y.W., R.D., J.Z., Z.L., J. Sun, Q.Z., C.d.C., S.W., Y.P., D.J.S., and G.C. contributed new reagents/analytic tools; and J.M., C.-W.C., and Z.R. wrote the paper.

Reviewers: R.C., University of California, San Diego; and L.Z., Beihang University.

The authors declare no conflict of interest.

[1]J.M., J. Shuai, and S.S. contributed equally to this work.

[2]To whom correspondence may be addressed. Email: cwchu@uh.edu or zren@uh.edu.

This article contains supporting information online at www.pnas.org/lookup/suppl/doi:10.1073/pnas.1711725114/-/DCSupplemental.

time is a function of carrier energy, E; temperature; and effective mass:

$$\tau \propto E^r T^s (m^*)^t. \quad \textbf{[2]}$$

Since τ varies for different scattering mechanisms, the mobility could be tuned by manipulating the carrier scattering mechanism.

Recently, a record high room temperature power factor of ∼106 $\mu W \cdot cm^{-1} \cdot K^{-2}$ was obtained in NbFeSb-based materials by optimizing the hot-pressing temperature (32). This high power factor originates from the noticeably improved mobility, which is due to the variation in the carrier scattering mechanism. Tamaki et al. (33) reported n-type Mg_3Sb_2-based materials with high thermoelectric performance via introducing extra Mg and Te doping, and similar results were also reported by Zhang et al. (34). Most recently, Shuai et al. (35) reported that substantial improvements in the room temperature Hall mobility and power factor were achieved in Nb/Te double-doped n-type Mg_3Sb_2-based materials. These materials showed mixed scattering due to ionized impurities and acoustic phonons, instead of being dominated by ionized impurity scattering. Therefore, these results unambiguously demonstrate that mobility can indeed be enhanced by tuning the carrier scattering mechanism.

The variation in the carrier scattering mechanism induced by Nb-doping in n-type Mg_3Sb_2-based materials is quite intriguing. It is natural to ask whether any other dopants have a similar effect and, more importantly, what are the underlying physics for such a phenomenon. Therefore, the motivation behind this work is to further investigate the carrier scattering mechanism in n-type Mg_3Sb_2-based materials. In the following discussion, it will be demonstrated that, in addition to Nb, transition-metal elements such as Fe, Co, Hf, and Ta show a similar effect in tuning the carrier scattering mechanism. In these cases, significant enhancements in the room temperature Hall mobility, μ_H (from ∼16 to ∼81 $cm^2 \cdot V^{-1} \cdot s^{-1}$), and power factor (from ∼5 to ∼13 $\mu W \cdot cm^{-1} \cdot K^{-2}$) are observed. A simultaneous reduction in the thermal conductivity is also achieved, and, finally, a ZT of ∼1.7 is obtained in $Mg_{3.1}Co_{0.1}Sb_{1.5}Bi_{0.49}Te_{0.01}$.

Results and Discussion

Based upon the composition of $Mg_{3.2}Sb_{1.5}Bi_{0.49}Te_{0.01}$, which showed the best thermoelectric performance among the Mg_3Sb_2-based materials from the report by Tamaki et al. (33), doping on the Mg site by different elements (Hf, V, Ta, Mo, W, Fe, Co, Ni, and Zn) was investigated. Among these elements, Fe, Co, Hf, and Ta have shown an effect similar to that of Nb in tuning the carrier scattering mechanism (Fig. 1*A*). Detailed thermoelectric properties of $Mg_{3.1}T_{0.1}Sb_{1.5}Bi_{0.49}Te_{0.01}$ (T = V, Mo, W, Ni, and Zn) are shown in *SI Appendix*, Fig. S1. For clarity, $Mg_{3.1}A_{0.1}Sb_{1.5}Bi_{0.49}Te_{0.01}$ (A = Fe, Co, Hf, and Ta) will be referenced as double-doped specimens in the following discussion.

Although a slight difference in the magnitude of electrical conductivity is observed between Tamaki et al.'s results (33) and our data for $Mg_{3.2}Sb_{1.5}Bi_{0.49}Te_{0.01}$, the temperature dependences for the two specimens are quite similar. In sharp contrast, the temperature dependences at lower temperatures for double-doped specimens are noticeably different from that of $Mg_{3.2}Sb_{1.5}Bi_{0.49}Te_{0.01}$. Temperature-dependent Hall mobility is shown in Fig. 1*B*, where distinctly different temperature dependences at lower temperatures can be observed and a substantial difference in Hall mobility is noted. The room temperature Hall mobility is ∼16 $cm^2 \cdot V^{-1} \cdot s^{-1}$ for $Mg_{3.2}Sb_{1.5}Bi_{0.49}Te_{0.01}$, while it is more than ∼50 $cm^2 \cdot V^{-1} \cdot s^{-1}$ for the double-doped specimens. $Mg_{3.1}Co_{0.1}Sb_{1.5}Bi_{0.49}Te_{0.01}$ shows the highest mobility of ∼81 $cm^2 \cdot V^{-1} \cdot s^{-1}$, an increase of more than 400% compared with that of $Mg_{3.2}Sb_{1.5}Bi_{0.49}Te_{0.01}$. It is important to note that the Hall mobilities are quite comparable at higher temperatures,

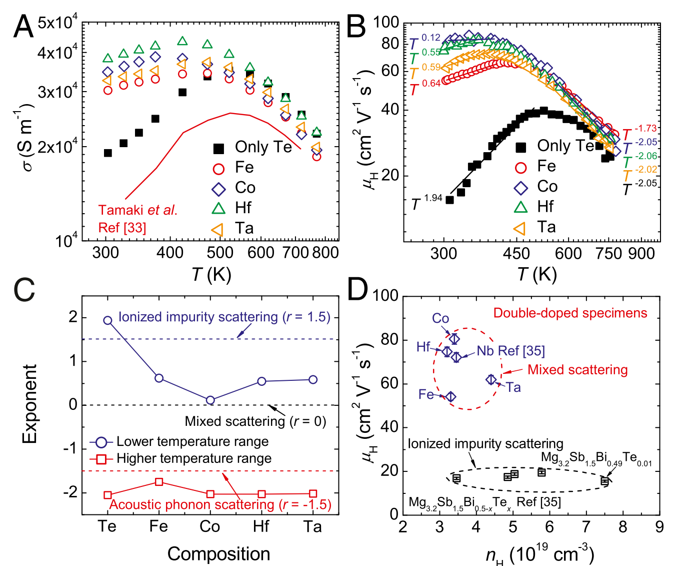

Fig. 1. Temperature-dependent electrical conductivity of (*A*), temperature-dependent Hall mobility of (*B*), composition-dependent temperature exponent of (*C*), and relationship between Hall carrier concentration, n_H, and Hall mobility for (*D*) $Mg_{3.2}Sb_{1.5}Bi_{0.49}Te_{0.01}$ and $Mg_{3.1}A_{0.1}Sb_{1.5}Bi_{0.49}Te_{0.01}$ (A = Fe, Co, Hf, and Ta). Data from ref. 33 in panel *A* and Nb data in panel *D* from ref. 35.

which should be ascribed mainly to the similar temperature dependence (i.e., the similar carrier scattering mechanism). This clearly indicates that the carrier scattering mechanism plays a critical role in the carrier mobility.

The relationship between the temperature exponent (derived from the Hall mobility) and composition is shown in Fig. 1*C*. In the lower temperature range, $Mg_{3.2}Sb_{1.5}Bi_{0.49}Te_{0.01}$ shows ionized impurity scattering, while the double-doped specimens are dominated by mixed scattering of ionized impurities and acoustic phonons. In the higher temperature range, all of the specimens are dominated by acoustic phonon scattering. The difference between the measured temperature exponent and the theoretical value for certain carrier scattering mechanisms (1.5 for ionized impurity scattering and −1.5 for acoustic phonon scattering) is noted, which could be partly ascribed to the assumptions involved in deriving the carrier scattering mechanism (e.g., it is usually assumed that the band is parabolic, but it could actually be a complex band structure). Fig. 1*D* shows the relationship between the Hall carrier concentration, n_H, and the Hall mobility. For $Mg_{3.2}Sb_{1.5}Bi_{0.5-x}Te_x$, where the ionized impurity scattering is dominant, the Hall mobility is quite low (less than ∼20 $cm^2 \cdot V^{-1} \cdot s^{-1}$) (35). Generally, the increased concentrations of ionized impurities and carriers will lead to enhanced ionized impurity scattering (36–38) and stronger electron-electron scattering (39–41), respectively. In other words, Hall mobility usually increases with decreasing the Hall carrier concentration. However, since the Hall carrier concentration of the double-doped specimens is similar to that of $Mg_{3.2}Sb_{1.5}Bi_{0.5-x}Te_x$ ($x < 0.01$), the noticeable enhancement in Hall mobility after doping of transition-metal elements cannot be ascribed simply to the reduced Hall carrier concentration.

Fig. 2*A* shows the temperature-dependent Seebeck coefficient, indicating that all of the double-doped specimens show slightly higher Seebeck coefficients than that of the $Mg_{3.2}Sb_{1.5}Bi_{0.49}Te_{0.01}$. The relationship between the Seebeck coefficient and the Hall carrier concentration can be understood well from the Pisarenko plot, as shown in Fig. 2*B*. $Mg_{3.2}Sb_{1.5}Bi_{0.49}Te_{0.01}$ and $Mg_{3.2}Sb_{1.5}Bi_{0.5-x}Te_x$ ($x < 0.01$) (35) show good agreement with the calculated Seebeck coefficient by considering the ionized impurity scattering. In contrast, all of the

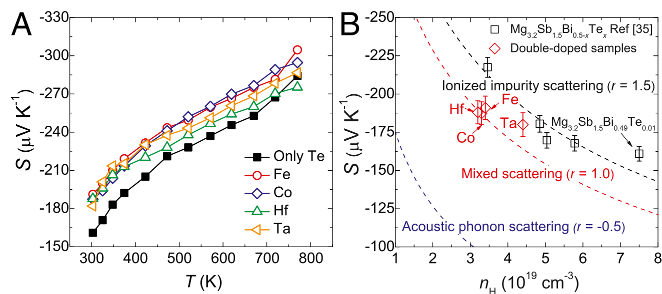

Fig. 2. Temperature-dependent Seebeck coefficient of (*A*) and relationship between Hall carrier concentration, n_H, and the Seebeck coefficient for (*B*) $Mg_{3.2}Sb_{1.5}Bi_{0.49}Te_{0.01}$ and $Mg_{3.1}A_{0.1}Sb_{1.5}Bi_{0.49}Te_{0.01}$ (*A* = Fe, Co, Hf, and Ta). The calculated density of states effective masses for all of the specimens are ~0.5 m_0. $Mg_{3.2}Sb_{1.5}Bi_{0.5\text{-}x}Te_x$ data in panel *B* from ref. 35.

double-doped specimens deviate from this prediction but are close to the mixed scattering (r = 1) result. At identical Hall carrier concentrations, ionized impurity scattering shows the highest Seebeck coefficient, followed by mixed scattering, with acoustic phonon scattering showing the lowest Seebeck coefficient. However, the Hall carrier concentration for Fe-, Co-, Hf-, and Ta-doped specimens (in the range between ~3 × 10^{19} cm^{-3} and ~4.4 × 10^{19} cm^{-3}) is lower than that of $Mg_{3.2}Sb_{1.5}Bi_{0.49}Te_{0.01}$ (~7.5 × 10^{19} cm^{-3}). This explains why slightly higher Seebeck coefficients are achieved in double-doped specimens. The difference in the Hall carrier concentration between $Mg_{3.2}Sb_{1.5}Bi_{0.49}Te_{0.01}$ and the double-doped specimens could be partially explained by the different amount of extra Mg. Our recent results indicate that extra Mg will change the carrier concentration in n-type Mg_3Sb_2-based materials, similar to the case of n-type Mg_2Sn-based materials (42), and detailed results will be reported elsewhere.

Due to the noticeably increased electrical conductivity and the slightly higher Seebeck coefficient, power factors are substantially improved for double-doped specimens at a lower temperature range (Fig. 3*A*). The room temperature power factor is ~5 μW·cm^{-1}·K^{-2} for $Mg_{3.2}Sb_{1.5}Bi_{0.49}Te_{0.01}$ but ~13 μW·cm^{-1}·K^{-2} for $Mg_{3.1}Hf_{0.1}Sb_{1.5}Bi_{0.49}Te_{0.01}$, an increase of ~160%. A comparison of the average power factor (calculated by the integration method between the temperatures of 300 and 773 K) is further shown in Fig. 3*B*, where the double-doped specimens show noticeable enhancement. The average power factor of $Mg_{3.1}Hf_{0.1}Sb_{1.5}Bi_{0.49}Te_{0.01}$ is ~19.7 μW·cm^{-1}·K^{-2}, which is ~29% higher than that of $Mg_{3.2}Sb_{1.5}Bi_{0.49}Te_{0.01}$ (~15.3 μW·cm^{-1}·K^{-2}). The relationship between the room temperature Hall mobility and the power factor is shown in Fig. 3*C*, where the effectively enhanced power factor in double-doped specimens should be mainly ascribed to the improved Hall mobility. The temperature exponent-dependent power factor is further shown in Fig. 3*D*. At a lower temperature range, the power factor of $Mg_{3.2}Sb_{1.5}Bi_{0.49}Te_{0.01}$ is much lower than that of double-doped specimens, which should be mainly due to the difference in the temperature exponent (i.e., the carrier scattering mechanism). On the contrary, the power factors at higher temperatures are quite comparable for all of the specimens, and this could be explained by having similar carrier scattering mechanisms. This demonstrates that power factors are also strongly dependent on the carrier scattering mechanism. More specifically, the power factors of n-type Mg_3Sb_2-based materials increase through the range of states from those dominated by ionized impurity scattering to those dominated by acoustic phonon scattering.

In addition to the enhanced power factors in doubled-doped specimens, lower thermal conductivity is achieved, as shown in Fig. 4*A*. The reduction in thermal conductivity could be partially ascribed to the phonon scattering by point defects. $Mg_{3.1}Co_{0.1}Sb_{1.5}Bi_{0.49}Te_{0.01}$ shows the lowest thermal conductivity, which could be due to the fact that Co has the highest solubility at the Mg site among all of the dopants (*SI Appendix*, Figs. S2 and S3). Owing to the substantially improved power factors and reduced thermal conductivities, *ZT*s have been effectively improved for the double-doped specimens, where a peak *ZT* of ~1.7 is obtained in $Mg_{3.1}Co_{0.1}Sb_{1.5}Bi_{0.49}Te_{0.01}$ (as shown in Fig. 4*B*). The engineering dimensionless *ZT* [$(ZT)_{eng}$] can be used to reliably and accurately predict the practical conversion efficiency (43). Therefore, the hot-side temperature (T_H)-dependent $(ZT)_{eng}$ is calculated as shown in Fig. 4*C*, where a noticeable increase in $(ZT)_{eng}$ is observed for the double-doped specimens. The $(ZT)_{eng}$ at the cold-side temperature (T_C) of 323 K and T_H of 773 K is ~0.67 for $Mg_{3.2}Sb_{1.5}Bi_{0.49}Te_{0.01}$ but ~0.97 for $Mg_{3.1}Co_{0.1}Sb_{1.5}Bi_{0.49}Te_{0.01}$, an increase of ~45%. The average *ZT* [$(ZT)_{avg}$] is calculated by the integration method over the temperature range of 300 to 773 K. Comparison of the $(ZT)_{avg}$ is shown in Fig. 4*D*, where the $(ZT)_{avg}$ is ~0.87 for $Mg_{3.2}Sb_{1.5}Bi_{0.49}Te_{0.01}$ but more than ~1.05 for double-doped specimens. A high $(ZT)_{avg}$ of ~1.19 is obtained in $Mg_{3.1}Co_{0.1}Sb_{1.5}Bi_{0.49}Te_{0.01}$, an increase of ~37% compared with $Mg_{3.2}Sb_{1.5}Bi_{0.49}Te_{0.01}$. Detailed composition-dependent thermoelectric properties of $Mg_{3.2-x}Co_xSb_{1.5}Bi_{0.49}Te_{0.01}$ (x = 0, x = 0.025, x = 0.05, x = 0.075, and x = 0.1) are also investigated, and an improvement in thermoelectric performance with an increased Co concentration can be observed (*SI Appendix*, Figs. S4 and S5).

To understand the reason for the variation in carrier scattering mechanisms, temperature-dependent Hall carrier concentrations for different specimens are compared, as shown in Fig. 5*A*. The Hall carrier concentrations of the double-doped specimens are either nearly temperature-independent (Fe and Co) or increase slightly with temperature (Hf and Ta). In striking contrast, $Mg_{3.2}Sb_{1.5}Bi_{0.49}Te_{0.01}$ shows an anomalous temperature-dependent Hall carrier concentration that decreases with temperature in the range of 300–500 K. Such unusual temperature dependence of the Hall carrier concentration has rarely been reported. To confirm the obtained results, the Hall carrier concentration was measured during both heating and cooling cycles, and similar results were observed (Fig. 5*B*). Repeated measurements were also conducted,

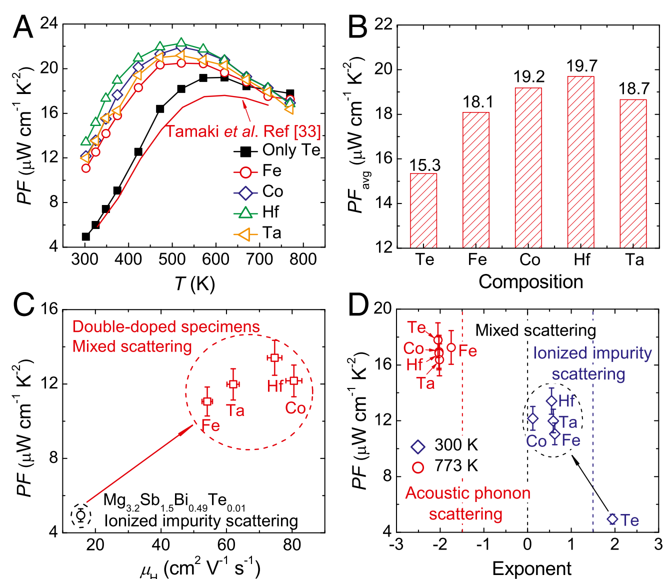

Fig. 3. Temperature-dependent power factor of (*A*), comparison of room temperature power factor among different specimens of (*B*), relationship between the Hall mobility and power factor for (*C*), and relationship between the temperature exponent and power factor for (*D*) $Mg_{3.2}Sb_{1.5}Bi_{0.49}Te_{0.01}$ and $Mg_{3.1}A_{0.1}Sb_{1.5}Bi_{0.49}Te_{0.01}$ (*A* = Fe, Co, Hf, and Ta). Data from ref. 33 in panel *A*.

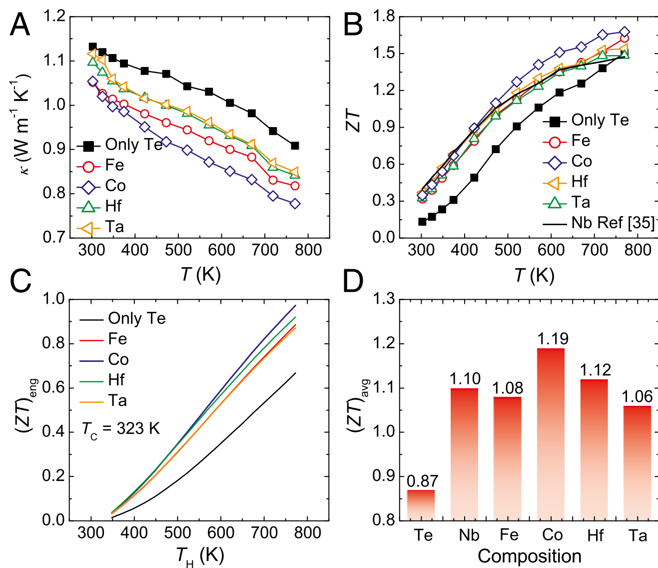

Fig. 4. Temperature-dependent thermal conductivity (*A*) and *ZT* of $Mg_{3.2}Sb_{1.5}Bi_{0.49}Te_{0.01}$ and $Mg_{3.1}A_{0.1}Sb_{1.5}Bi_{0.49}Te_{0.01}$ (*B*) (*A* = Fe, Co, Hf, and Ta). Calculated $(ZT)_{eng}$ at a cold-side temperature (T_C) of 323 K (*C*) and comparison of $(ZT)_{avg}$ between $Mg_{3.2}Sb_{1.5}Bi_{0.49}Te_{0.01}$ and $Mg_{3.1}A_{0.1}Sb_{1.5}Bi_{0.49}Te_{0.01}$ (*D*) (*A* = Nb, Fe, Co, Hf, and Ta). Nb data in panel *B* from ref. 35.

with similar results (*SI Appendix*, Fig. S6). It should be noted that our results are different from those of Tamaki et al. (33); however, the reason for such a difference is unclear at this stage.

For $Mg_{3.2}Sb_{1.5}Bi_{0.49}Te_{0.01}$, the ionized impurity scattering dominates in the same temperature range (Fig. 1*B*) in which the Hall carrier concentration decreases with temperature. Therefore, the ionized impurity scattering should be closely related to the anomalous temperature dependence of the Hall carrier concentration. More importantly, since the Hall carrier concentration of $Mg_{3.2}Sb_{1.5}Bi_{0.49}Te_{0.01}$ is highly reversible during the heating and cooling cycles, this suggests a thermodynamic reason for such a unique temperature dependence of the Hall carrier concentration.

According to the calculation by Tamaki et al. (33), in both the Mg-poor and Mg-rich conditions, negatively charged Mg vacancies are the most stable kinds of defects. It is worth noting that neutral-state vacancies can easily become charged due to their unsaturated bonding capabilities (e.g., dangling bonds). These capabilities facilitate the transfer of an electronic charge between the host matrix and the vacancy, and often occur to the point that the vacancy becomes fully ionized. The degree (different charge states) and direction of electron transfer (toward or away from the vacancy) naturally depend upon the electron richness of the host, as quantified by the host's Fermi energy in the vicinity of the vacancy (44). The negatively charged Mg vacancy means that the neutral-state Mg vacancy always tends to acquire electrons from the host. In the Mg-rich condition of our specimens, −2 and −3 are the most stable charges for the Mg vacancy.

The ratio of charged Mg vacancy (V_{Mg}^{2-} and V_{Mg}^{3-}) to neutral Mg vacancy V_{Mg}^{0} can be described as follows (44, 45):

$$c_{V_{Mg}^{2-}} \Big/ c_{V_{Mg}^{0}} = \exp\left[-\left(E_{V_{Mg}^{2-}} - 2E_F\right) \Big/ kT\right], \quad [3]$$

$$c_{V_{Mg}^{3-}} \Big/ c_{V_{Mg}^{0}} = \exp\left[-\left(E_{V_{Mg}^{3-}} + E_{V_{Mg}^{2-}} - 3E_F\right) \Big/ kT\right], \quad [4]$$

where $c_{V_{Mg}^{0}}$ is the concentration of V_{Mg}^{0}, $c_{V_{Mg}^{2-}}$ is the concentration of V_{Mg}^{2-}, $c_{V_{Mg}^{3-}}$ is the concentration of V_{Mg}^{3-}, $E_{V_{Mg}^{2-}}$ is the acceptor level energy of V_{Mg}^{2-}, $E_{V_{Mg}^{3-}}$ is the acceptor level energy of V_{Mg}^{3-}, and E_F is the Fermi level energy.

The thermal equilibrium concentration of the neutral Mg vacancy is expressed as follows (46):

$$c_{V_{Mg}^{0}} = c_0 \exp\left[-g_{V_{Mg}^{0}} \Big/ kT\right], \quad [5]$$

where c_0 is the crystal atom density and $g_{V_{Mg}^{0}}$ is the Gibbs free energy of formation of V_{Mg}^{0}.

Therefore, the concentration of charged Mg vacancies is strongly temperature-dependent. In fact, the charged vacancies usually tend to increase with temperature. The charged Mg vacancies will inevitably change with the measured Hall carrier concentration according to the charge neutrality condition (45):

$$n = c_{Te} - 2c_{V_{Mg}^{2-}} - 3c_{V_{Mg}^{3-}} + p. \quad [6]$$

Clearly, the carrier concentration depends upon the concentrations of dopant (Te) and charged defects (V_{Mg}^{2-} and V_{Mg}^{3-}), as well as minority carrier (hole) concentration. To explain the temperature dependence of the Hall carrier concentration in $Mg_{3.2}Sb_{1.5}Bi_{0.49}Te_{0.01}$, schematic views are shown in Fig. 5*B*. The neutral Mg vacancy captures the electron and becomes ionized during the heating process, and it releases the electron and returns to the neutral state during the cooling process. The reversible ionization and deionization of the Mg vacancy with respect to temperature will induce the corresponding variation in the Hall carrier concentration.

To prove the existence of Mg vacancies in the n-type Mg_3Sb_2-based materials, neutron powder diffraction was conducted for $Mg_{3.2}Sb_{1.5}Bi_{0.49}Te_{0.01}$ and $Mg_{3.1}Co_{0.1}Sb_{1.5}Bi_{0.49}Te_{0.01}$. The Rietveld refinements for the two specimens are shown in the *SI Appendix*, Fig. S7. To achieve stable and converging refinement for the neutron powder diffraction of the samples, some assumptions were made, and the details can be found in *SI Appendix*. The refinement for $Mg_{3.2}Sb_{1.5}Bi_{0.49}Te_{0.01}$ indicates that the Mg1 site, [1/3, 2/3, 0.6292(7)], is 100% occupied, while the Mg2 site, (0, 0, 0), is only 89 ± 2% occupied. This implies that Mg vacancies indeed exist in $Mg_{3.2}Sb_{1.5}Bi_{0.49}Te_{0.01}$ and that they preferentially locate at the Mg2 site with a concentration of 11 ± 2%. Likewise, in $Mg_{3.1}Co_{0.1}Sb_{1.5}Bi_{0.49}Te_{0.01}$, the Mg1 site, [1/3, 2/3, 0.6236(9)], was found to be fully occupied. Co only dopes onto the Mg2 site, and the total occupancy of this site was found to be 91 ± 2% (*SI Appendix*, Fig. S7 and Table S1). This implies that the Co doping reduces the concentration of Mg vacancies, which could explain why the transition-metal–doped samples do not show the anomalous temperature dependence of the Hall carrier concentration (Fig. 5*A*). In addition, it is worth noting that a proposed Mg interstitial site, (0, 0, 1/2), (33) did not fit well to the data, and refinement of the occupancy tended toward zero. Therefore, the location of the extra Mg needs to be further investigated.

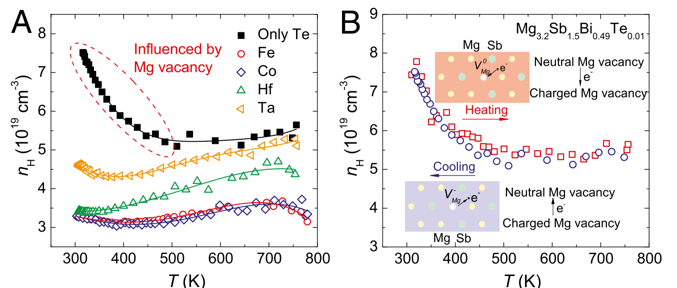

Fig. 5. Temperature-dependent Hall carrier concentrations of $Mg_{3.2}Sb_{1.5}Bi_{0.49}Te_{0.01}$ and $Mg_{3.1}A_{0.1}Sb_{1.5}Bi_{0.49}Te_{0.01}$ (*A*) and the Hall carrier concentration of $Mg_{3.2}Sb_{1.5}Bi_{0.49}Te_{0.01}$ during heating and cooling cycles (*B*). (*A* = Fe, Co, Hf, and Ta) (*Insets*) Schematic views of ionization and deionization of the Mg vacancy.

One critical question is how the unique temperature dependence of the Hall carrier concentration relates to the variation in the carrier scattering mechanism. In principle, the carrier mobility, when ionized impurity scattering is dominant, can be expressed as follows (39):

$$\mu_I = 2^{7/2}/\pi^{3/2}K^2(kT)^{3/2}/(m^*)^{1/2}e^3N_I[\ln(1+b) - b/1+b]^{-1},$$
$$b = 6/\pi Km^*k^2T^2/n\hbar^2e^2, \quad [7]$$

where K is the dielectric constant, N_I is the ionized impurity concentration, k is the Boltzmann constant, and $\hbar$ is the reduced Planck's constant.

According to the Pisarenko plot (Fig. 2*B*), all of the specimens can be described well by considering different carrier scattering mechanisms with an identical m^*, which means the m^* should remain unchanged or quite similar after doping. It was previously assumed that the improved mobility is due to an increased dielectric constant after the transition-metal doping (35). Indeed, the dielectric constant is sensitive to the trace amounts of dopants in various material systems (47–53). However, this seems not to be the case for the n-type Mg_3Sb_2-based materials, where the calculated dielectric constants for Mg_3Sb_2 and $Mg_3Sb_{1.5}Bi_{0.5}$ are quite comparable considering the fact that up to 25% of the Sb has been replaced by Bi (*SI Appendix*, Table S2).

Therefore, the variation in the Hall mobility should not come from the variation in the material's intrinsic parameters (m^* and K). It should be noted that the ionized impurity concentration can be approximated to be the carrier concentration only when one type of dopant is present. In the case of multiple types of dopants, the ionized impurity concentration could be larger than the carrier concentration. In the n-type Mg_3Sb_2-based materials, the ionized impurities include both the ionized Te atoms and the charged Mg vacancies. The Rietveld refinement of neutron powder diffraction and the temperature-dependent Hall carrier concentration show that the double-doped specimens have lower concentrations of charged Mg vacancies. The noticeable difference in thermoelectric properties between the doubled-doped specimens and $Mg_{3.2}Sb_{1.5}Bi_{0.49}Te_{0.01}$ indicates that charged Mg vacancies play a central role in the carrier scattering mechanism, and hence the thermoelectric properties of n-type Mg_3Sb_2-based materials. In other words, by reducing the concentration of charged Mg vacancies, the ionized impurity scattering in $Mg_{3.2}Sb_{1.5}Bi_{0.49}Te_{0.01}$ changes to the mixed scattering in double-doped specimens.

In both NbFeSb (32) and n-type Mg_3Sb_2-based materials (35), the carrier scattering mechanism at a lower temperature shifted from extrinsic scattering mechanisms (i.e., grain boundary scattering, ionized impurity scattering) toward acoustic phonon scattering. Although different approaches (i.e., increasing hot-pressing temperature, doping) were used, the key idea of manipulating the carrier scattering mechanisms is identical, and relies on the control of defects (i.e., grain boundaries, Mg vacancies). Therefore, to apply this strategy to other material systems, it is first necessary to identify the defect that is responsible for the dominant carrier scattering mechanism and then to try to control it. In fact, since the dominant carrier scattering mechanism (especially in the lower temperature range) could be different for different materials, this concept should be applicable to a variety of other material systems for enhancing thermoelectric performance.

Conclusions

Ionized impurity scattering in the n-type Mg_3Sb_2-based materials is investigated further. Our results demonstrate that by doping transition-metal elements such as Fe, Co, Hf, and Ta at the Mg site of $Mg_{3.2}Sb_{1.5}Bi_{0.49}Te_{0.01}$, the dominant ionized impurity scattering at a lower temperature changes to a mixed scattering of acoustic phonons and ionized impurities, thus noticeably improving the Hall mobility and power factor. A simultaneous reduction in thermal conductivity is achieved, and, finally, a ZT of ~1.7 is obtained in $Mg_{3.1}Co_{0.1}Sb_{1.5}Bi_{0.49}Te_{0.01}$. Our work demonstrates that the carrier scattering mechanism could play a vital role in the thermoelectric properties of the material, and the concept of tuning the carrier scattering mechanism should be widely applicable to a variety of material systems.

Experimental Section

Synthesis. Mg turnings (99.98%; Alfa Aesar), Bi pieces (99.99%; Alfa Aesar), Sb shots (99.8%; Alfa Aesar), Te pieces (99.999%; Alfa Aesar), Hf crystals (99.9%; Altantic Metals & Alloys), V powders (99.5%; Alfa Aesar), Ta powders (99.9%; Alfa Aesar), Mo powders (99.95%; Alfa Aesar), W powders (99.9%; Alfa Aesar), Fe powders (99%; Alfa Aesar), Co powders (99.5%; Alfa Aesar), Ni powders (99%; Alfa Aesar), and Zn powders (99.9%; Alfa Aesar) were weighed according to the composition of $Mg_{3.2-x}A_xSb_{1.5}Bi_{0.49}Te_{0.01}$ (A = Hf, V, Ta, Mo, W, Fe, Co, Ni, and Zn). The elements were loaded into a stainless-steel ball-milling jar in a glove box under an argon atmosphere with an oxygen level below 0.1 ppm. The materials were ball-milled for 10 h and then loaded into a graphite die with an inner diameter of 12.7 mm. The graphite die with the loaded powder was then removed from the glove box and immediately sintered by hot pressing at 923 K under a pressure of ~80 MPa for 2 min. The hot-pressed disks are about 2–3 mm thick.

Thermoelectric Property Characterizations. All of the samples were cut into pieces with dimensions of about 2 mm × 2 mm × 12 mm for simultaneous electrical resistivity and Seebeck coefficient characterizations under an He atmosphere (ZEM-3; ULVAC Riko). Thermal conductivity, $\kappa = dDC_p$, was calculated using the measured density, d, (*SI Appendix*, Table S3) determined by the Archimedean method, thermal diffusivity, D, (*SI Appendix*, Fig. S8*A*) by determined by the laser flash method (LFA 457; Netzsch), and specific heat, C_p, (*SI Appendix*, Fig. S8*B*) by differential scanning calorimetry (DSC 404 C; Netzsch). The Hall coefficient, R_H, was measured at room temperature on a commercial system (PPMS; Quantum Design) using a four-probe configuration, with the magnetic field sweeping between +3 T and −3 T and an electrical current between 10 mA and 20 mA. The temperature-dependent Hall measurement was conducted under a reversible magnetic field of 1.5 T using the Van der Pauw technique from 300 to 773 K. The Hall carrier concentration, n_H, and the carrier mobility, μ, were calculated via the relations $n_H = 1/(e{\cdot}R_H)$ and $\mu = R_H/\rho$. Thermoelectric properties show good thermal stability during the cooling and heating cycles (*SI Appendix*, Fig. S9).

Structure and Phase Composition. The phase composition of the samples was characterized by X-ray diffraction (PANalytical X'pert PRO diffractometer with a Cu K_a radiation source).

Neutron Diffraction. Neutron powder diffraction data were taken on samples of $Mg_{3.2}Sb_{1.5}Bi_{0.49}Te_{0.01}$ and $Mg_{3.1}Co_{0.1}Sb_{1.5}Bi_{0.49}Te_{0.01}$ in an ambient environment on HB-2A at the High Flux Isotope Reactor at Oak Ridge National Laboratory. A GE (115) monochromator (λ = 1.54 Å) and open – 21′ – 12′ collimation corresponding to before the monochromator, before the sample, and before the detector, respectively, were used. Pattern refinement was performed using the Rietveld method in FullProf (54), and the details for the refinement are shown in *SI Appendix*, Fig. S7 and Table S1.

First Principles Density Functional Calculations. Dielectric tensors were calculated using the density functional perturbation theory as implemented in the VASP code (55). We used the generalized gradient approximation of Perdew et al. (56) and standard projector-augmented wave pseudopotentials. A planewave cutoff of 520 eV was used for the valence wavefunctions, and the Mg 2p and Bi 5d orbitals were included as valence states. We used relaxed lattice parameters and atomic coordinates for the calculations of dielectric tensors in both Mg_3Sb_2 and $Mg_3Sb_{1.5}Bi_{0.5}$.

ACKNOWLEDGMENTS. The work performed at the University of Houston and the University of Missouri is supported by the Solid State Solar-Thermal Energy Conversion Center, an Energy Frontier Research Center funded by the US Department of Energy, Office of Science, Office of Basic Energy Sciences under Award DE-SC0001299, as well as by US Air Force Office of Scientific Research Grant FA9550-15-1-0236, the T. L. L. Temple Foundation, the John J. and Rebecca Moores Endowment, and the State of Texas through the Texas Center

for Superconductivity at the University of Houston. Research conducted at the Oak Ridge National Laboratory's High Flux Isotope Reactor was sponsored by the Scientific User Facilities Division, Office of Basic Energy Sciences, US Department of Energy. The work performed at Tongji University is funded by the National Natural Science Foundation of China (Grants 51422208 and 11474219).

1. DiSalvo FJ (1999) Thermoelectric cooling and power generation. *Science* 285:703–706.
2. Bell LE (2008) Cooling, heating, generating power, and recovering waste heat with thermoelectric systems. *Science* 321:1457–1461.
3. Snyder GJ, Toberer ES (2008) Complex thermoelectric materials. *Nat Mater* 7:105–114.
4. Pei Y, Wang H, Snyder GJ (2012) Band engineering of thermoelectric materials. *Adv Mater* 24:6125–6135.
5. Yang J, et al. (2016) On the tuning of electrical and thermal transport in thermoelectrics: An integrated theory-experiment perspective. *njp Computational Materials* 2:15015.
6. Mao J, Liu Z, Ren Z (2016) Size effect in thermoelectric materials. *njp Quantum Materials* 1:16028.
7. Ioffe AF (1957) *Semiconductor Thermoelements and Thermoelectric Cooling* (Infosearch, London).
8. Ioffe AV, Ioffe AF (1960) Thermal conductivity of semiconductor solid solutions. *Sov Phys Solid State* 2:719–728.
9. Dismukes JP, Ekstrom L, Steigmeier EF, Kudman I, Beers DS (1964) Thermal and electrical properties of heavily doped Ge-Si alloys up to 1300 K. *J Appl Phys* 35: 2899–2907.
10. Yang J, Meisner GP, Chen L (2004) Strain field fluctuation effects on lattice thermal conductivity of ZrNiSn-based thermoelectric compounds. *Appl Phys Lett* 85: 1140–1142.
11. Mao J, et al. (2017) Thermoelectric properties of n-type ZrNiPb-based half-Heuslers. *Chem Mater* 29:867–872.
12. Kim SI, et al. (2015) Thermoelectrics. Dense dislocation arrays embedded in grain boundaries for high-performance bulk thermoelectrics. *Science* 348:109–114.
13. Kim HS, Kang SD, Tang Y, Hanus R, Snyder GJ (2016) Dislocation strain as the mechanism of phonon scattering at grain boundaries. *Mater Horiz* 3:234–240.
14. Chen Z, et al. (2017) Vacancy-induced dislocations within grains for high-performance PbSe thermoelectrics. *Nat Commun* 8:13828.
15. Chen Z, et al. (2017) Lattice dislocations enhancing thermoelectric PbTe in addition to band convergence. *Adv Mater* 29:1606768.
16. Poudel B, et al. (2008) High-thermoelectric performance of nanostructured bismuth antimony telluride bulk alloys. *Science* 320:634–638.
17. Mao J, Wang YM, Liu ZH, Ge BH, Ren ZF (2017) Phonon scattering by nanoscale twin boundaries. *Nano Energy* 32:174–179.
18. Zhao LD, et al. (2016) Enhanced thermoelectric properties in the counter-doped SnTe system with strained endotaxial SrTe. *J Am Chem Soc* 138:2366–2373.
19. Pei Y, et al. (2011) Convergence of electronic bands for high performance bulk thermoelectrics. *Nature* 473:66–69.
20. Liu W, et al. (2012) Convergence of conduction bands as a means of enhancing thermoelectric performance of n-type $Mg_2Si_{(1-x)}Sn_{(x)}$ solid solutions. *Phys Rev Lett* 108:166601.
21. Pei YZ, LaLonde AD, Wang H, Snyder GJ (2012) Low effective mass leading to high thermoelectric performance. *Energy Environ Sci* 5:7963–7969.
22. Fu CG, Zhu TJ, Liu YT, Xie HH, Zhao XB (2014) Band engineering of high performance p-type FeNbSb based half-Heusler thermoelectric materials for figure of merit $zT > 1$. *Energy Environ Sci* 8:216–220.
23. Heremans JP, et al. (2008) Enhancement of thermoelectric efficiency in PbTe by distortion of the electronic density of states. *Science* 321:554–557.
24. Meng XF, et al. (2017) Grain boundary engineering for achieving high thermoelectric performance in n-type Skutterudites. *Adv Energy Mater* 7:1602582.
25. Mao J, et al. (2015) High thermoelectric power factor in Cu–Ni alloy originate from potential barrier scattering of twin boundaries. *Nano Energy* 17:279–289.
26. Nishio Y, Hirano T (1997) Improvement of the efficiency of thermoelectric energy conversion by utilizing potential barriers. *Jpn J Appl Phys* 36:170–174.
27. Kishimoto K, Koyanagi T (2002) Preparation of sintered degenerate n-type PbTe with a small grain size and its thermoelectric properties. *J Appl Phys* 92:2544–2549.
28. Wang S, et al. (2015) On intensifying carrier impurity scattering to enhance thermoelectric performance in Cr-doped $Ce_yCo_4Sb_{12}$. *Adv Funct Mater* 25:6660–6670.
29. Zebarjadi M, et al. (2011) Power factor enhancement by modulation doping in bulk nanocomposites. *Nano Lett* 11:2225–2230.
30. Yu B, et al. (2012) Enhancement of thermoelectric properties by modulation-doping in silicon germanium alloy nanocomposites. *Nano Lett* 12:2077–2082.
31. Ravich II (2013) *Semiconducting Lead Chalcogenides* (Springer, New York).
32. He R, et al. (2016) Achieving high power factor and output power density in p-type half-Heuslers $Nb_{1-x}Ti_xFeSb$. *Proc Natl Acad Sci USA* 113:13576–13581.
33. Tamaki H, Sato HK, Kanno T (2016) Isotropic conduction network and defect chemistry in $Mg_{3+\delta}Sb_2$-based layered Zintl compounds with high thermoelectric performance. *Adv Mater* 28:10182–10187.
34. Zhang J, et al. (2017) Discovery of high-performance low-cost n-type Mg_3Sb_2-based thermoelectric materials with multi-valley conduction bands. *Nat Commun* 8:13901.
35. Shuai J, et al. (2017) Tuning the carrier scattering mechanism to effectively improve the thermoelectric properties. *Energy Environ Sci* 10:799–807.
36. Long D, Myers J (1959) Ionized-impurity scattering mobility of electrons in silicon. *Phys Rev* 115:1107–1118.
37. Chattopadhyay D, Queisser H (1981) Electron scattering by ionized impurities in semiconductors. *Rev Mod Phys* 53:745–768.
38. Brooks H (1955) Theory of the electrical properties of germanium and silicon. *Adv Electron Electron Phys* 7:85–182.
39. Debye P, Conwell E (1954) Electrical properties of n-type germanium. *Phys Rev* 93: 693–706.
40. Hartman R (1969) Temperature dependence of the low-field galvanomagnetic coefficients of bismuth. *Phys Rev* 181:1070–1086.
41. Thompson A (1975) Electron-electron scattering in TiS_2. *Phys Rev Lett* 35:1786–1789.
42. Liu W, et al. (2011) Optimized thermoelectric properties of Sb-doped $Mg_{2(1+z)}Si_{0.5-y}Sn_{0.5}Sb_y$ through adjustment of the Mg content. *Chem Mater* 23:5256–5263.
43. Kim HS, Liu W, Chen G, Chu CW, Ren Z (2015) Relationship between thermoelectric figure of merit and energy conversion efficiency. *Proc Natl Acad Sci USA* 112: 8205–8210.
44. Seebauer EG, Kratzer MC (2006) Charged point defects in semiconductors. *Mater Sci Eng Rep* 55:57–149.
45. Tan TY, You HM, Gösele UM (1993) Thermal equilibrium concentrations and effects of negatively charged Ga vacancies in n-type GaAs. *Appl Phys A Mater Sci Process* 56: 249–258.
46. Tan TY (1991) Point defect thermal equilibria in GaAs. *Mater Sci Eng B* 10:227–239.
47. Van Dover R (1999) Amorphous lanthanide-doped TiO_x dielectric films. *Appl Phys Lett* 74:3041–3043.
48. Joshi P, Cole M (2000) Mg-doped $Ba_{0.6}Sr_{0.4}TiO_3$ thin films for tunable microwave applications. *Appl Phys Lett* 77:289–291.
49. Wu J, Nan C-W, Lin Y, Deng Y (2002) Giant dielectric permittivity observed in Li and Ti doped NiO. *Phys Rev Lett* 89:217601.
50. Chong K, et al. (2004) Improvement of dielectric loss tangent of Al_2O_3 doped $Ba_{0.5}Sr_{0.5}TiO_3$ thin films for tunable microwave devices. *J Appl Phys* 95:1416–1419.
51. Tomida K, Kita K, Toriumi A (2006) Dielectric constant enhancement due to Si incorporation into HfO_2. *Appl Phys Lett* 89:142902.
52. Kwon S, et al. (2008) The effect of Cr_2O_3, Nb_2O_5 and ZrO_2 doping on the dielectric properties of $CaCu_3Ti_4O_{12}$. *Mater Lett* 62:633–636.
53. Dar MA, Batoo KM, Verma V, Siddiqui W, Kotnala R (2010) Synthesis and characterization of nano-sized pure and Al-doped lithium ferrite having high value of dielectric constant. *J Alloys Compd* 493:553–560.
54. Rodríguez-Carvajal J (1993) Recent advances in magnetic structure determination by neutron powder diffraction. *Physica B* 192:55–69.
55. Kresse G, Furthmüller J (1996) Self-interaction correction to density functional approximation for many electron systems. *Phys Rev B* 54:11169.
56. Perdew JP, Burke K, Ernzerhof M (1996) Generalized gradient approximation made simple. *Phys Rev Lett* 77:3865–3868.

PNAS PNAS PNAS